



# Nonlinear analysis of voltage dynamics in a polymer electrolyte fuel cell due to two-phase channel flow



Michael B. Burkholder, Nicholas S. Siefert, Shawn Litster\*

Carnegie Mellon University, 5000 Forbes Avenue, Pittsburgh, PA 15213, United States

## HIGHLIGHTS

- Non-linear analysis of chaotic polymer electrolyte fuel cell voltage.
- Correlation dimension, Kolmogorov entropy, & Hurst and Lyapunov exponents.
- Non-linear statistic related to operating condition and two-phase flow regime.
- Computationally efficient reduced-order statistics identified.
- Future applications feedback for embedded fuel cell controllers.

## ARTICLE INFO

### Article history:

Received 31 January 2014

Received in revised form

23 April 2014

Accepted 25 April 2014

Available online 20 May 2014

### Keywords:

Polymer electrolyte fuel cell

Nonlinear analysis

Chaos

Water management

Two-phase flow

## ABSTRACT

More efficient water management techniques are required to decrease the cost of polymer electrolyte fuel cell (PEFC) systems while maintaining robust performance. In this study, we use nonlinear statistical analysis of experimental data to characterize PEFC dynamics under conditions where water accumulation in the cathode air-delivery microchannels causes decreases in performance accompanied by chaotic fluctuations. Using experimental PEFC voltage signals, we estimate chaotic invariants indicative of the degrees of freedom of the dynamics (the correlation dimension) and the instability of the dynamics (the Kolmogorov entropy). We find that these invariants decrease with increasing gas flow commensurate with greater fuel cell current and air stoichiometric ratio, and that they are indicative of the channel two-phase flow regime. We correlate the Lyapunov exponents of the one-dimensional voltage return map and the Hurst exponents of the voltage time series with the chaotic invariants for use in future PEFC water management and control strategies. In addition, we examine the relationships between the invariants estimated from the voltage signal and the two-phase friction multiplier calculated from measured cathode pressure drop in order to distinguish the distinct dynamics of two-phase channel flow.

© 2014 Elsevier B.V. All rights reserved.

## 1. Introduction

Polymer electrolyte fuel cells (PEFCs) are electrochemical engines that convert hydrogen and oxygen to electricity, with byproducts of water and heat. The ability of sustainably- and renewably-produced hydrogen to provide low emission electricity makes it an attractive alternative to the combustion of limited-supply, carbon-based fuels like petroleum and coal. Because PEFCs offer high power density and quick startup owing to their sub 100 °C operating temperature, they remain promising for use in transportation applications.

While the product water exhaust makes PEFCs attractive as clean engines, it also poses water management problems that reduce system efficiency and hinder robustness of operation [1]. In the PEFC cathode, water is produced according to the oxygen reduction reaction in which oxygen, usually provided by air flow, combines with hydrogen ions and electrons. A certain amount of water is desirable to hydrate the polymer electrolyte membrane, thereby decreasing its ionic resistance [2]. However, too much water can increase the resistance to oxygen diffusion, leading to oxygen starvation and large mass transport overpotentials.

The ability to effectively remove surplus water from the cathode with a low parasitic cost is confounded by the air delivery mechanism and two-phase flow effects under certain operating conditions. State of the art air delivery flow fields are composed of arrays of parallel microchannels which deliver oxygen to the active fuel cell area and remove excess water. To achieve low parasitic costs, it

\* Corresponding author.

E-mail addresses: [mburkhol@andrew.cmu.edu](mailto:mburkhol@andrew.cmu.edu) (M.B. Burkholder), [nicholas.siefert@netl.doe.gov](mailto:nicholas.siefert@netl.doe.gov) (N.S. Siefert), [litster@andrew.cmu.edu](mailto:litster@andrew.cmu.edu) (S. Litster).

is desirable to use low air flow rates in channels with low hydraulic resistance. However, the air momentum that makes positive contributions to the hydraulic resistance also removes liquid water through nonlinear momentum transfer. Hence, low air flow rates allow water to accumulate in the microchannels, thereby reducing the effective cathode active area and the fuel cell power output.

For high current densities, neutron radiography visualization has shown that the water accumulation in the cathode microchannels is relatively insensitive to the air stoichiometric ratio  $\xi$  [3], which is the ratio of the air flow rate delivered to that required for the reaction. At low current densities, however, the water accumulation and PEFC performance become more sensitive to  $\xi$  because the two-phase flow regime in the microchannels tends towards slug/plug flow when the channel superficial air and water velocities ( $u_g$  and  $u_l$ , respectively) are low [4,5]. In arrays of parallel channels, the complete blockage of individual channels by water plugs allows air flow to divert from plugged channels to open channels, following the path of least resistance [6]. The diverted flow leaves flooded channels plugged until enough pressure builds up to clear them, resulting in voltage instability and fluctuations, and power loss [7,8] (see Fig. 1). While the channel plurality [8] in a single lab-scale fuel cell may prove manageable, the large numbers of parallel channels present in fuel cell stacks used to power an automobile (>10,000) introduce many additional degrees of freedom and instability into the system's dynamics.

To avoid detrimental instability from water accumulation, operation in the slug flow regime is minimized in favor of annular film flow [5], which can be aided through geometric and material flow field design optimization. Different geometric flow field designs have been investigated, and while interdigitated channels have been shown to effectively remove liquid water [9], they produce much larger pressure drops than the conventional parallel/serpentine channel flow fields. To promote stable liquid water removal via annular film or corner flow, hydrophilic flow field materials may be used [10,11] as well as smaller channel dimensions that increase the gas velocity. Even with these flow field design optimizations, effective water removal is driven by supplying excessive air flow rates at multiple times the

stoichiometric flow rate, resulting in high parasitic load on the fuel cell output, especially during the low-power idling and startup conditions.

One class of PEFC water management techniques uses fault detection. Output indicative of fuel cell health is monitored, and corrective water purging action is taken when the output indicates that the cathode is flooded. Many different diagnostics have been proposed for fault detection. One such linear fault detection scheme monitors the levels and oscillation frequencies of fuel cell voltage and resistance, stack voltage, pressure drop, and load [12]. When any of these signals breaches a predefined threshold, the air flow rate is pulsed to drive out liquid water. The amplitude response of voltage to small output pressure oscillations, indicated by the voltage variance, has also been proposed as a diagnostic for cathode flooding [13]. Additionally, electrochemical impedance spectroscopy has been employed to indicate cathode health [14]. Fuel cell dehydration shows a strong impedance response across a broad frequency range, while cathode flooding shows a much weaker impedance response across a limited frequency range. Both of the last two techniques require additional hardware to periodically excite the PEFC system, with the latter also requiring frequency response analysis electronics.

To improve upon such fault detection techniques, the signal being monitored and the threshold values can be optimized in a way that is consistent with the nonlinearities of PEFC water accumulation and removal dynamics. Nonlinear chaotic behavior has long been observed in chemical reaction kinetics, like the classic Belousov–Zhabotinsky reaction [15]. The complex PEFC water balance involves two-phase flow in parallel microchannels with electrochemical feedback, resulting in highly nonlinear and chaotic dynamics. While linear indicators like voltage oscillation frequency and magnitude may indicate changes in the PEFC dynamics, they do not account for potential nonlinear differences (e.g. in stability) between dynamics with similar linear oscillation characteristics. To address the shortcomings of linear analysis, nonlinear techniques have been used to analyze similar chaotic systems. For instance, calculation of chaotic invariants like Kolmogorov entropy has been shown to indicate two-phase flow regime changes [16], and nonlinear statistics have been shown to provide early defluidization warning in a fluidized bed [17]. Thus, instability induced by changes in system parameters with long dynamical timescales, such as fuel cell temperature and pressure, is potentially detectable using nonlinear statistics before it is apparent from linear statistics. It is also possible to stabilize unstable dynamics with minimal effort using chaos control techniques without changing the system parameters [18]. Bubbling has been controlled with chaos control in a fluidized bed [17], and chaos has been observed and controlled in electrochemical reactions [19].

The purpose of this paper is to provide a framework for understanding the nonlinear, chaotic dynamics of PEFC water management. We apply the first nonlinear time series analysis to PEFC instabilities to investigate how the presence of two-phase flow affects invariant quantities indicative of the degrees of freedom and the stability of the dynamics. We also propose new nonlinear voltage statistics that indicate the dynamical stability and are much less expensive to compute than the traditional chaotic invariants.

## 2. Method

This section presents the nonlinear analysis methodology that we used in this work and insight into its physical interpretation. Our implementation of the equations and algorithms has been validated on well-characterized nonlinear and stochastic systems like the Lorenz system [20] and Brownian motion, respectively.

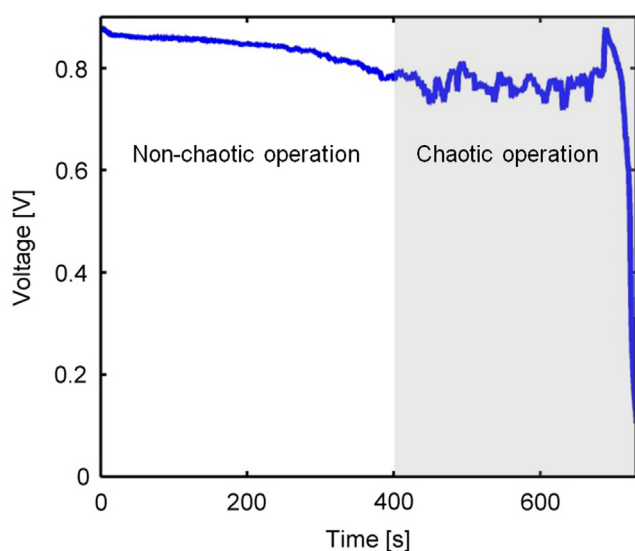


**Fig. 1.** Voltage signal of an operating PEFC beginning from a purged condition. As water accumulates, voltage output decreases and chaotic voltage fluctuations are introduced (around 400 s) before the cathode completely floods and voltage is lost (around 700 s).

## 2.1. State space

Due to a lack of analytical tools, common analysis techniques for nonlinear systems focus on the geometrical properties of the system state-space attractor. When nonlinear differential state equations are integrated, they yield a trajectory through the state space over time, where each orthogonal coordinate on the trajectory is a state as a function of time. The region of state space to which the trajectory is confined is the system attractor.

Experimentally, the state space can be reconstructed from the observed time series of a single state,  $x(t)$  [21]. The technique, called time-delay embedding, creates a time series of  $m$ -dimensional embedded vectors,  $\mathbf{x}(t)$ , where each coordinate is the observed time series lagged a time delay  $\tau$  behind the previous coordinate, Eq. (1). Such a reconstructed vector space preserves the topology of the system state space, and hence the geometrical properties of the attractor, provided that enough dimensions, in this case time-delays, are used.

$$\mathbf{x}(t) = [x(t), x(t - \tau), x(t - 2\tau), \dots, x(t - (m - 1)\tau)] \quad (1)$$

Using the embedded space, invariant properties of the state space, *i.e.* quantities that are the same for all valid state space reconstructions, may be estimated with neighborhood statistics. Neighborhood statistics are used to determine not only how a single point on the trajectory evolves over time, but also how similar states within a neighborhood of distance  $r$  evolve over time. For non-chaotic systems, the evolution of similar states is also similar and neighborhood statistics provide little additional information. In chaotic systems, due to the sensitive dependence on initial conditions, similar states exhibit exponentially differing time evolution and thus neighborhood statistics are necessary to quantify attractor properties. This is because the evolution of a single initial condition is not indicative of the evolution of other initial conditions, even similar ones. Fig. 2 shows a three-dimensional section of the >3D chaotic time-delay embedded attractor for the voltage signal in Fig. 1.

Confidently estimating state space invariants requires accurate neighborhood statistics over a large range of neighborhood sizes. For an experimentally measured, time-delay embedded state space, finite amounts of data can limit statistical accuracy at large  $r$ . In

addition, the presence of dynamical and measurement noise scatters the points around the attractor manifold, limiting accuracy at small  $r$ . Due to the computational intensity of the estimation algorithms, it is often impractical to use large amounts of data, making noise reduction desirable to increase the accessible range of  $r$ .

Low-pass filters commonly used for noise reduction are based on the assumption that frequency components from noise are linearly additive to the signal. In nonlinear systems, power input at one frequency is distributed among many frequencies, violating this assumption. Thus, we used a nonlinear noise reduction (NNR) algorithm [22] to filter the voltage signals. The noise reduction, schematically depicted in two dimensions in Fig. 3, is performed in the reconstructed state space. For each point in the  $m$ -dimensional space ( $m = 2$  in Fig. 3), a hyper ellipsoid is fit to the neighborhood. Noise is reduced by projecting the point towards the local, linearized attractor manifold approximated by the neighborhood. The  $q$  smallest principal axes of the hyper ellipsoid are assumed to be noise components ( $q = 1$  in Fig. 3), and each point is projected toward the  $m-q$ -dimensional attractor manifold by removing the noise components ( $m-q = 1$  in Fig. 3). The procedure is iterated for convergence.

## 2.2. Fractal dimensions

One invariant of the state space that we estimated is the attractor dimension, which is the active degrees of freedom available to the dynamics. The attractor dimension typically has a fractal value in the presence of chaotic dynamics, and for this reason chaotic attractors are often called strange attractors.

The topological dimension is an integer describing how many coordinates are necessary to specify a unique point in any object, including dynamical attractors. The topological dimension of an attractor is how many effective states contribute to the dynamics, or the number of state space dimensions in which the system dynamics are free to move. A stable  $m$ -dimensional state space trajectory will typically be confined to an integer-dimensional attractor (of dimension  $n$ ) in a subspace of the state space ( $n < m$ ), with a higher  $n$  being associated with more complex dynamics. Should a manifold in the state space become unstable, as through a

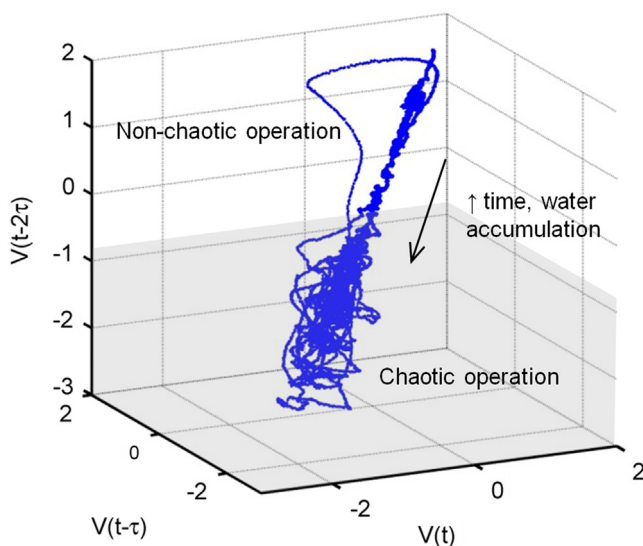


Fig. 2. Time-delay embedded attractor of the voltage signal in Fig. 1 with  $m = 3$ . The strange attractor in the chaotic region has a fractal dimension.

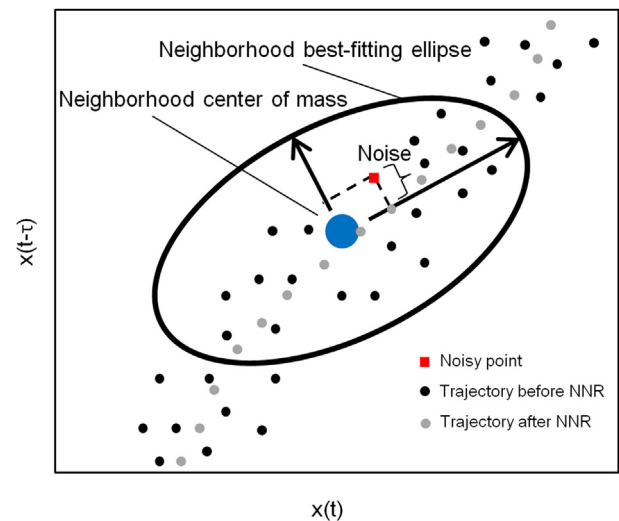


Fig. 3. Schematic of the nonlinear noise reduction procedure, wherein each point is projected towards the attractor manifold approximated by the primary axes of the neighborhood best-fitting ellipsoid. Here, the noise component of the square point is depicted, as well as the trajectory before and after the noise reduction procedure.

bifurcation, the dynamics become chaotic and the attractor gains additional degrees of freedom in the direction of instability, resulting in a fractally-dimensioned attractor. From the point of view of the integer topological dimension, the chaotic attractor does not entirely fill another dimension of state space and thus still has a dimension of  $n$ , when in reality the fractal attractor fills more space than its topological dimension of  $n$  but less space than  $n + 1$  dimensions.

For this reason it is necessary to generalize the topological dimension to account for the additional degrees of freedom of the dynamics. One such generalization is the correlation dimension,  $D_2$ , a straightforward estimate of attractor dimension in a time-delay embedded state space [23]. Estimation of  $D_2$  is achieved by computing correlation sums  $C(r)$  from Eq. (2), which represent how the average attractor density (or number of neighbors) changes as a function of the neighborhood radius  $r$ . The power law scaling of  $C(r)$  with  $r$  then yields the correlation dimension:  $C \propto r^{D_2}$ , which gives an integer value for attractors with integer dimensions and a decimal value for attractors with fractal dimensions. In Eq. (2),  $\Theta$  is the Heaviside step function,  $N$  is the total number of points, and since we don't want to count points that are in the neighborhood due to temporal correlations,  $T$  is the length of the temporal correlation. By averaging the number of points within the neighborhood of size  $r$ , we then have the correlation sums as a function of  $r$ , and also as a function of  $m$  through the embedding procedure.

$$C(r, m) = \frac{2}{(N-T)(N-T-1)} \sum_{i=1}^N \sum_{j=i+T+1}^N \Theta(r - \|\mathbf{x}(t_i) - \mathbf{x}(t_j)\|) \quad (2)$$

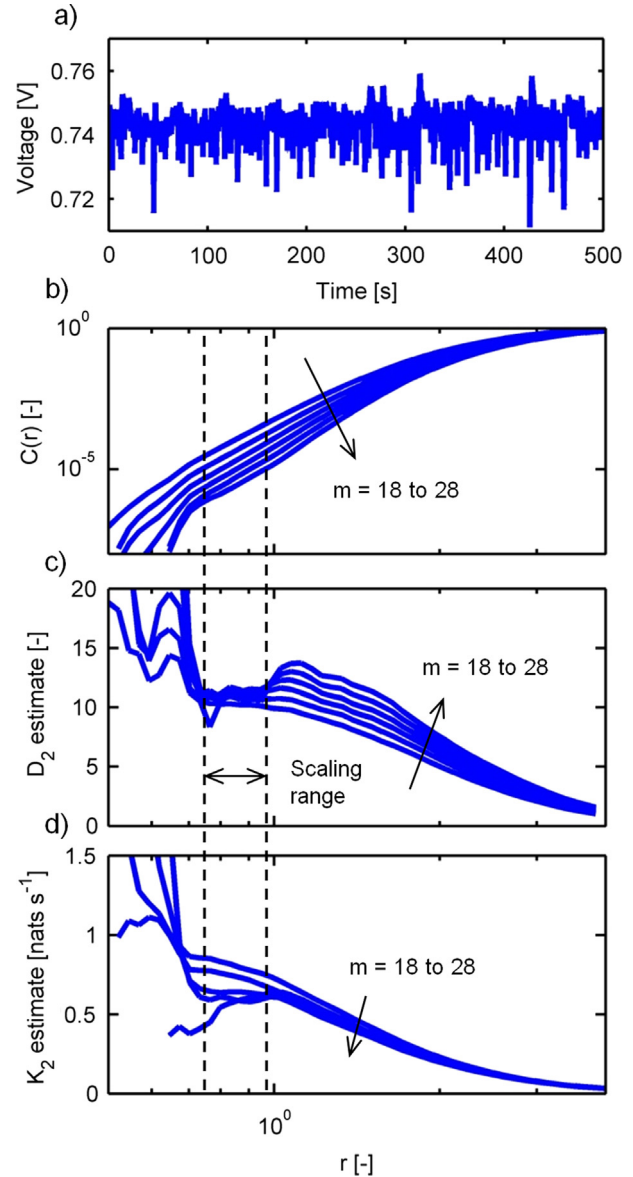
Due to the finite amount of data and sampling frequency, the power law scaling necessary to make an estimate of  $D_2$  occurs over a limited range of  $r$ , called the scaling range. A dimension estimate should only be made when there is clear linearity in the log–log plot of  $C(r)$ , which is apparent from a plateau in the local slopes. Because noise can also produce a plateau in  $C(r)$  at the embedding dimension  $m$ , a plateau for a confident  $D_2$  estimate should be witnessed for all correlation sums with embedding dimensions high enough to accommodate the attractor.

Fig. 4 shows an example of estimating  $D_2$  from a PEFC voltage signal. The power law scaling of the correlation sums yields a  $D_2$  estimate of approximately 10 for a current density of  $0.1 \text{ A cm}^{-2}$  and  $\xi = 1.5$ , indicating the presence of high-dimensional chaos. In our analysis, we normalized the delay vectors by the standard deviation of the signal and so  $r$  is the unitless number of standard deviations.

### 2.3. Information entropy

Another invariant that we estimate is the Kolmogorov entropy. It is an entropy in the information theory sense in the fact that it is a measure of the amount of information about prior states needed to specify the current state. In a stable, non-chaotic system where the states evolve in a predictable manner, no Kolmogorov entropy is present. For random systems where no amount of prior information can be used to predict the next outcome, there is infinite Kolmogorov entropy. For chaotic systems with sensitive dependence on initial conditions due to the exponential divergence of initially similar states, there is a positive, finite Kolmogorov entropy.

The Kolmogorov entropy  $K$  is computed by dividing the state space into hypercubes and considering the joint probabilities with which the trajectory visits the hypercubes. With an experimental time series, it is much easier to calculate the order-2 Renyi entropy  $K_2$ , which is positive for chaotic systems and is upper bounded by  $K$



**Fig. 4.** a) Voltage time series at  $0.1 \text{ A cm}^{-2}$ ,  $\xi = 1.5$ ; b) correlation sums computed from the normalized voltage time series for  $m = 18, 20, 22, 24, 26$ , and  $28$ ; c) local slopes of the correlation sums yielding a  $D_2$  estimate of approximately 10; d) Kolmogorov entropy estimates from the correlation sums yielding a  $K_2$  estimate of about  $0.6 \text{ nats s}^{-1}$ . Such estimates may only be made from convergence in the power law scaling range indicated by a plateau in the correlation sum slopes.

[24]. The computation, described by Eq. (3), can be made directly from the correlation sums for varying embedding dimensions  $m$ , where  $n$  is the integer distance between consecutive values of  $m$ .

$$K_2 = \lim_{m \rightarrow \infty} \lim_{r \rightarrow 0} \frac{1}{n\tau} \log \left( \frac{C(r, m)}{C(r, m+n)} \right) \quad (3)$$

Similar to  $D_2$  estimation, a confident  $K_2$  estimate should only be made over the scaling range when power law scaling is apparent in the correlation sums. While the power law scaling itself is not a sufficient condition to indicate chaos, a positive  $K_2$  value such as that shown in Fig. 4 is sufficient [24].

The Kolmogorov entropy is also the sum of the positive Lyapunov exponents (LEs,  $\lambda$ ). The Lyapunov exponent spectrum is the exponential rates of convergence (negative) or divergence



(positive) over time of a small volume of initial conditions on the attractor. The spectrum has as many exponents as the attractor dimension, but usually only the positive exponents which characterize the level of instability in the system are of interest. Chaotic systems have at least one positive Lyapunov exponent, which gives rise to the sensitive dependence on initial conditions through exponential divergence of initially similar states.

The units of entropy depend on the base of the logarithm used in Eq. (3). Herein, we have used the natural logarithm, making our entropy estimates in units of nats  $s^{-1}$ , where a nat is the natural unit of entropy or information. Comparatively, we have estimated the LEs from a map with a base-2 logarithm (see next section), yielding units of bits  $iteration^{-1}$ . One nat is approximately 1.44 bits.

#### 2.4. Maps

As mentioned earlier, when performing certain neighborhood statistics to determine invariant properties of the attractor, we do not consider points that are within the neighborhood because of temporal correlations. These are points that lie on the same trajectory pass through the neighborhood rather than on a prior or returning pass. In Eq. (2), the temporal correlation time is given by  $T\Delta t$ , where  $\Delta t$  is the sampling interval. We are not interested in points within the temporal correlation time because they contain redundant information, *i.e.* invariant attractor quantities are exhibited in how fast and how close trajectories return to the original neighborhood after they have left it.

A common technique used in nonlinear analysis to eliminate redundant data is to reduce the order of the state space by converting the time series ‘flow’ to a map. A map is a rule of the type  $\mathbf{x}_{n+1} = f(\mathbf{x}_n)$ , and the goal is to choose the map such that the discarded data between  $\mathbf{x}_n$  and  $\mathbf{x}_{n+1}$  is redundant. A popular map choice is the Poincaré map, which is created by choosing the  $\mathbf{x}_n$  as the intersections of the state space trajectory with a section in the state space. The choice of section, called the Poincaré section, thus defines the mapping, and the dynamics of the Poincaré map are confined to the Poincaré section, a lower-dimensional manifold than the attractor.

One choice of Poincaré section is to use the consecutive maxima or minima in the time series  $x(t)$  as the  $\mathbf{x}_n$ . This one-dimensional map is called a return map. Using the return map, parameter choices like the time delay  $\tau$  and temporal correlation length  $T$  are eliminated. Furthermore, estimation of the maximal Lyapunov exponent from the divergence of initially close peaks, *i.e.* peaks of similar magnitude, becomes much more straightforward. For two initially similar peaks separated by a distance of  $d_0$ , the local Lyapunov exponent is given by  $\lambda = \log_2 d_1/d_0$  where  $d_1$  is the distance between the peaks after one iteration on the map (see Fig. 5). The average of the local Lyapunov exponents of many initially similar peaks can then be used to estimate the maximal Lyapunov exponent of the map. Later in this paper, we demonstrate the correlation between the Lyapunov exponent estimate of the voltage return map and the dynamical entropy of the time-delay embedded state space.

#### 2.5. Diffusion analysis

Another way to quantify fractal structure in a signal is through computation of the Hurst exponent [25], which was originally formulated to study the long-term storage capacity of reservoirs fed by unpredictable sources like rainfall and has since been used to detect instability in financial markets prior to crashes [26], among other applications. For diffusion-like processes, the Hurst exponent  $H$  describes the power law scaling between the distance over which the signal  $x$  diffuses and time  $t$ , *i.e.*  $\langle \Delta x^2 \rangle \propto \Delta t^{2H}$ , where the angle brackets denote an average. For the special case where  $H = 0.5$ , the

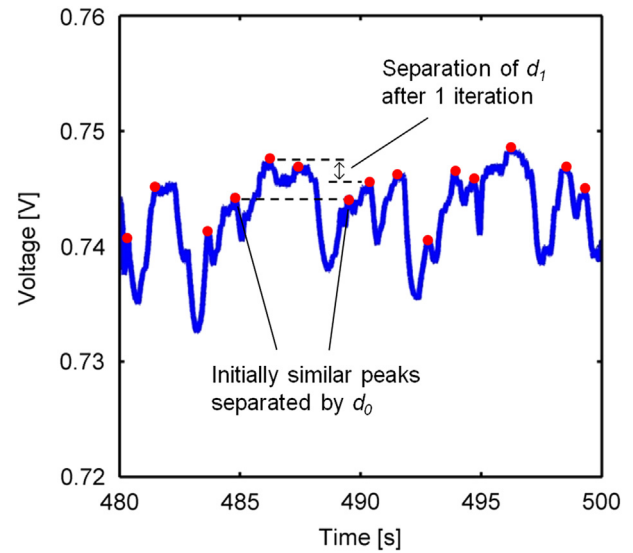


Fig. 5. Voltage return map (dots) for 20 s of the 0.1 A  $cm^{-2}$ ,  $\xi = 1.5$  voltage signal. The local Lyapunov exponent is estimated from the divergence of initially similar peaks.

diffusion scales with the square root of time and is an uncorrelated random walk (*i.e.* Brownian motion). A value of  $H$  different from 0.5 indicates some memory in the signal, with  $H > 0.5$  indicating positive autocorrelation and  $H < 0.5$  indicating negative autocorrelation. A value of  $H = 1$  is yielded by a smooth signal typical of ballistic motion [27], while  $H = 0$  is given by signals where adjacent values lie on opposite sides of the mean.

Estimation of the Hurst exponent from a stationary signal may be achieved using diffusion analysis. For this purpose, a bounded signal  $x(t)$ , such as PEFC voltage, is interpreted as diffusion increments to extend the scaling. Thus the signal is first integrated to yield a diffusion-like quantity:  $y(t) = \int_0^t x(t')dt'$ . As shown in Eq. (4), the root mean squared distance over which the integrated signal diffuses ( $F$ ) is computed for varying time windows of length  $\tau$ , where the angle brackets indicate an average over consecutive windows. Power law scaling between  $F$  and  $\tau$  gives the Hurst exponent estimate:  $F \propto \tau^H$ .

$$F(\tau) = \sqrt{\langle (y(t+\tau) - y(t))^2 \rangle} \quad (4)$$

These analysis techniques for time series are nonlinear because they make no assumptions about linearity in the physics that produce the time series. When we reconstruct an embedded state space from a PEFC voltage signal, we preserve the invariant nonlinear dynamical properties of the entire PEFC system, including the two-phase flow dynamics of cathode water accumulation and removal. The dimension and entropy invariants, as well as the Lyapunov exponents of the return map, are all related to the overall stability of the dynamics, a property of concern for optimal control. While the PEFC stability may have some correlation with linear statistics like voltage mean and variance, there is no guarantee that the mapping is one-to-one. Hence, we estimate these invariants for a PEFC to characterize how the dynamical stability changes with operating conditions. We also estimate the Hurst exponent as a nonlinear indication of the autocorrelation, or memory, of the dynamics.

### 3. Experimental

We gathered data from 50  $cm^2$  active area PEFC hardware (Fuel Cell Technologies, Inc., Albuquerque, NM) where the cathode flow

field plate was custom designed and machined from a carbon-loaded vinyl ester (BMC 940-8649, Bulk Molding Compounds, Inc., Chicago, IL) with a fully parallel channel flow field to add degrees of freedom and enhance instabilities from low air velocities (Fig. 6). This allows better simulation of full-scale stack dynamics than a traditional lab-scale serpentine flow field. The cathode plate had 52 parallel channels covering the 7 cm by 7 cm active area, each 0.5 mm wide by 0.3 mm deep, corresponding to a channel plurality of  $\chi = 1 \text{ cm}^{-2}$  ( $\chi^* = 1.6 \times 10^{-3}$ ) [8]. Automotive stacks are expected to have values in the range of  $\chi^* \approx 1.3 \times 10^{-3}$  [28]. The inlet and outlet header dimensions were much larger than the channel dimensions to minimize flow maldistribution from pressure drop along the header. The headers had pressure taps inserted flush with the sidewalls to record pressure measurements across the cathode flow field with a differential pressure transducer (PX-409, Omega Engineering, Inc., Stamford, CT). The anode flow field was a 3-pass serpentine design (see Fig. 1 in Ref. [7]).

The membrane-electrode assembly was an 18  $\mu\text{m}$  Gore membrane with 0.4/0.4 mg Pt  $\text{cm}^{-2}$  catalyst loading (W. L. Gore and Associates, Inc, Elkton, MD). The gas diffusion layer was MRC U105 carbon paper (Mitsubishi Rayon Co, Ltd, Tokyo, Japan) with a microporous layer.

Fuel cell testing was conducted using a commercial fuel cell test stand (FCT-150S, Bio-Logic SAS, Claix, France) with temperature, humidity, load, and reactant gas flow control. The fuel cell and reactant gas temperatures were held constant at 55 °C for all experiments to achieve 100% relative humidity (RH). The temperature was lower than the typical 80 °C to mimic the severe flooding observed during startup. The fuel cell backpressure was atmospheric. Before each experiment, residual liquid water was purged from the fuel cell with 1000 mlpm reactant flow rates held for 2 min. The fuel cell was allowed >10 min to equilibrate before the data was gathered, and the anode flow rate was held constant at a stoichiometric ratio of 2.

Galvanostatic voltage data and differential pressure data were gathered for current densities ranging from 0.1 to 0.3  $\text{A cm}^{-2}$  and air stoichiometric ratios,  $\xi$ , from 1.25 to 2 at a frequency of 100 Hz using a data acquisition board (>10 G $\Omega$  input impedance) connected to a computer with LabVIEW software (National Instruments Corporation, Austin, TX). Post processing of the data and the nonlinear analysis were done with custom codes run using

MATLAB software (MathWorks, Natick, MA). Computational processing was accelerated by writing and compiling the neighborhood search algorithms in C, as well as by parallelizing the code.

## 4. Results

To characterize the overall fuel cell performance, we measured galvanostatic polarization curves at the experimental conditions for air stoichiometric flow rates of  $\xi = 1.25, 1.5$ , and 2. The VI curves are shown in Fig. 7. At low current densities, there is a reduction in voltage with decreasing  $\xi$  attributable to channel flooding. The presence of liquid water in the channels at low current densities is typical of a two-phase slug flow regime, and decreases the effective active area of the fuel cell resulting in voltage loss. There is a slight recovery of the voltage loss for  $\xi = 1.25$  at 0.4  $\text{A cm}^{-2}$  as the amount of liquid water present in the channels decreases. At high current densities, the concentration overpotential becomes evident. The high-current polarization at  $\xi = 1.25$  may also have effects from the presence of liquid water in the catalyst and gas diffusion layers, causing increased resistance to oxygen diffusion.

### 4.1. Chaotic dynamics

We conducted galvanostatic potentiometry experiments to identify fuel cell operating conditions under which the output voltage signal is chaotic. Due to the degrees of freedom provided by the parallel air delivery microchannels, we expected conditions that lead to slug and plug channel flow regimes to yield the most chaotic dynamics. Noting the scalings  $u_g \propto \xi i$  and  $u_l \propto i$ , where  $i$  is the current, two-phase flow regime maps [4,5] indicate that low-current, low- $\xi$  conditions are most chaotic, consistent with our own experimental data.

Fig. 8 shows 20 s durations of the voltage signals for current densities of 0.1  $\text{A cm}^{-2}$ , 0.2  $\text{A cm}^{-2}$ , and 0.3  $\text{A cm}^{-2}$ . For each current density, voltage time series were collected for air stoichiometric ratios of  $\xi = 1.25, 1.5, 1.75$ , and 2. The computed nonlinear statistics presented later are based on 500 s durations of the voltage time series after the equilibration time. At a constant current density, the voltage fluctuation magnitude decreases as  $\xi$  is increased, indicating more effective removal of liquid water due to the increased

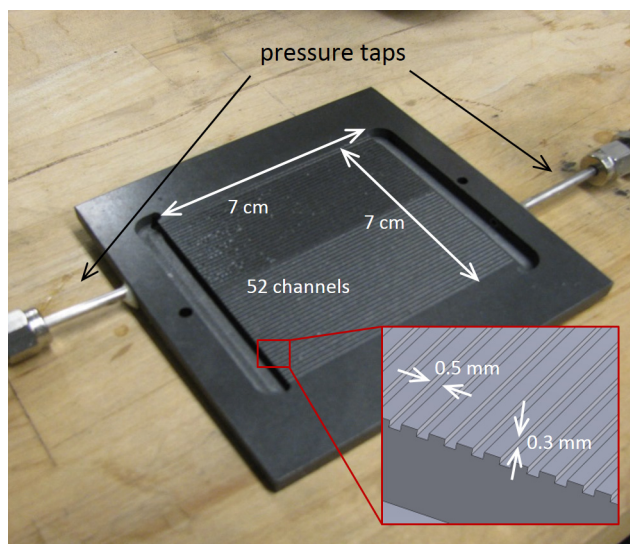


Fig. 6. Custom, fully-parallel experimental cathode flow field with pressure taps in the headers.

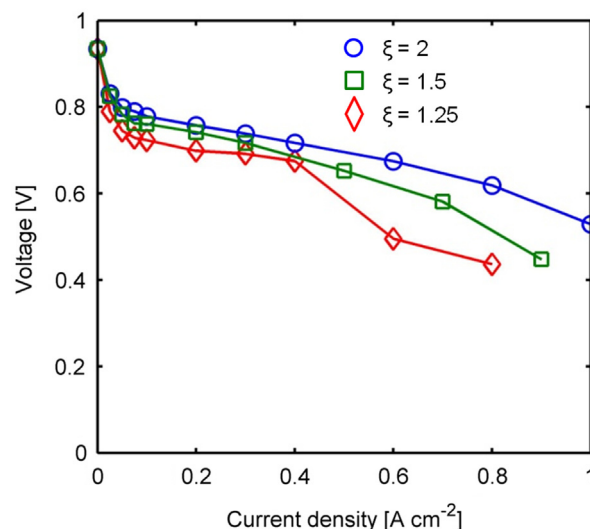
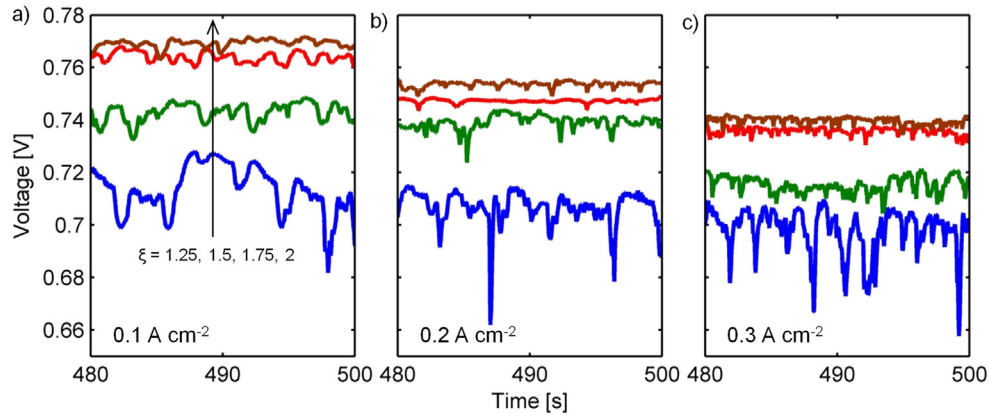


Fig. 7. Galvanostatic VI curves at experimental conditions with  $\xi = 1.25$  (bottom), 1.5 (middle), and 2 (top).



**Fig. 8.** Voltage time series at  $\xi = 1.25, 1.5, 1.75$ , and  $2$  (bottom to top) for varying current densities of a)  $0.1 \text{ A cm}^{-2}$ , b)  $0.2 \text{ A cm}^{-2}$ , and c)  $0.3 \text{ A cm}^{-2}$ . Fluctuation magnitude decreases with increasing  $\xi$ , and fluctuation frequency increases with increasing current.

air flow rate [8]. As the current density increases, and hence the air and water flow rates, so does the voltage fluctuation frequency.

For the same experimental conditions, we averaged the differential two-phase cathode pressure drop,  $\Delta P_{2\phi}$  (the subscript  $2\phi$  is used to denote two-phase), over the 500-s durations used for the nonlinear analysis and plotted them versus  $u_g$  in Fig. 9. For laminar, single-phase flow of the gas, we expect a linear increase in  $\Delta P_g$  with  $u_g$  (the subscript  $g$  denotes a gas-only flow) from the theory of flow in pipes. However, for two-phase flow the pressure drop is commonly modeled as  $\Delta P_{2\phi} = \Delta P_g \Phi_{2\phi}$ , where  $\Phi_{2\phi}$  is the two-phase friction multiplier. Due to the nonlinearities of two-phase flow,  $\Phi_{2\phi}$  is an empirical parameter that corrects the gas-only pressure drop for the presence of another phase, and is thus dependent upon the two-phase flow regime. The decrease in  $\Delta P_{2\phi}$  with increasing  $u_g$  at  $0.1 \text{ A cm}^{-2}$  can be attributed to a decrease in  $\Phi_{2\phi}$  such as would occur in the onset of the transition to a flow regime with a lower pressure drop. The nonlinear trend at  $0.2 \text{ A cm}^{-2}$  can be likewise attributed to a decrease in  $\Phi_{2\phi}$ . At  $0.3 \text{ A cm}^{-2}$ , we see a linear trend indicating an

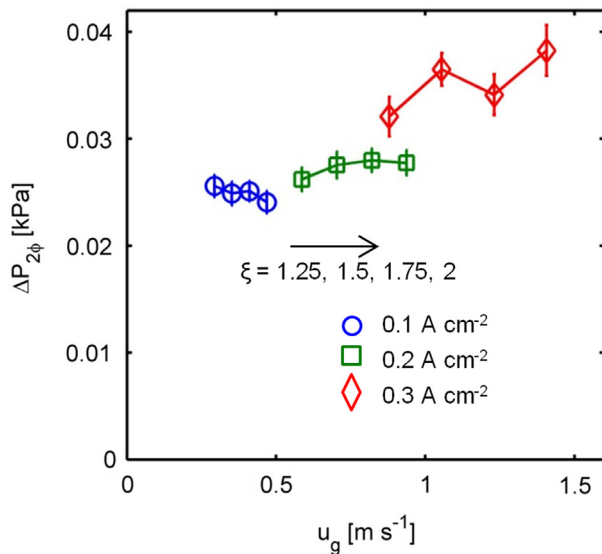


**Fig. 9.** Differential two-phase cathode pressure  $\Delta P_{2\phi}$  vs. the superficial air velocity  $u_g$  for current densities of  $0.1 \text{ A cm}^{-2}$ ,  $0.2 \text{ A cm}^{-2}$ , and  $0.3 \text{ A cm}^{-2}$ , each with  $\xi = 1.25, 1.5, 1.75$ , and  $2$ . The values shown are averages over the 500-s durations used for the nonlinear analysis, and the error bars are the standard deviations. The nonlinearities of two-phase flow can be seen in the  $0.1 \text{ A cm}^{-2}$  and  $0.2 \text{ A cm}^{-2}$  differential pressures, which do not increase linearly with  $u_g$  as expected for single-phase flow.

approximately constant  $\Phi_{2\phi}$  and hence a stable two-phase flow regime like annular flow. For a discussion of  $\Phi_{2\phi}$ , see Section 5.1.

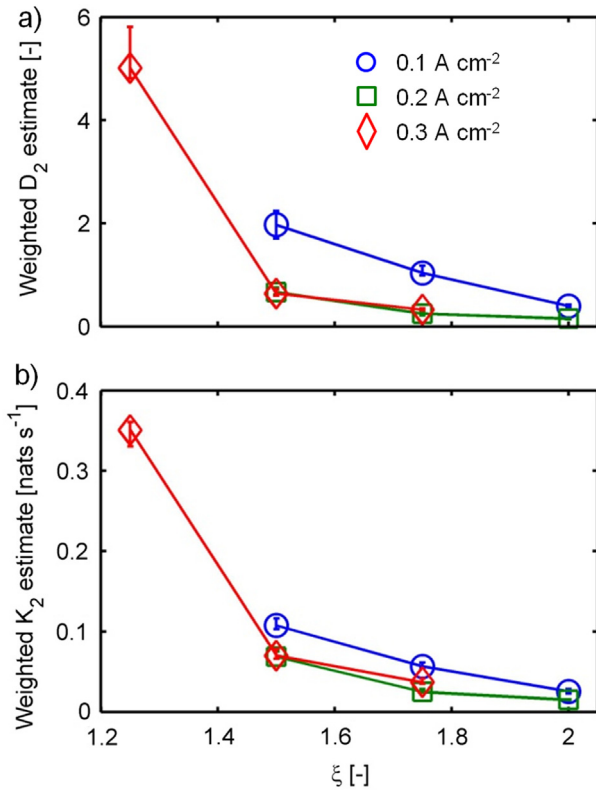
After filtering the 500-s durations of the voltage signals with the nonlinear noise reduction algorithm from Section 2.1, we computed correlation sums to use in the estimation of the chaotic invariants  $D_2$  and  $K_2$ . The removal of sufficient noise to reveal power law scaling proved to be sensitive to the parameters chosen for the noise reduction, which require some *a priori* knowledge of the attractor dimension and the noise level. To account for the spurious effects of noise, which has a greater impact at lower scaling ranges and causes overestimation of the invariants [29], we weighted our estimates linearly by the median value of the (un-normalized) scaling range (for a discussion of the weighting, see Section 5.1).

Fig. 10 plots the weighted  $D_2$  and  $K_2$  estimates as a function of current density and  $\xi$ , where the error bars cover the variability in  $C(r, m)$  over the scaling range. The conditions for which no estimates are shown are those that did not yield convincing power law scaling in the correlation sums. This estimate uncertainty could result from an insufficient amount of data, the presence of noise, or the lack of chaotic behavior.

The positive entropy  $K_2$  is a sufficient condition to indicate chaotic dynamics [24], and the fractal dimension  $D_2$  further supports this conclusion while providing us with the embedding dimensions required to compute accurate nonlinear statistics. We observed that the weighted  $D_2$  and  $K_2$  estimates for  $0.2$  and  $0.3 \text{ A cm}^{-2}$  fall on the same curve, while those for  $0.1 \text{ A cm}^{-2}$  remain slightly higher, at least for  $\xi = 1.5$  and  $1.75$ . The estimates show a reduction in the active degrees of freedom and the entropy for increasing  $\xi$ , indicating that the dynamics are more stable with higher air flow rates consistent with more effective cathode water removal. The small reduction in  $D_2$  and  $K_2$  from  $0.1 \text{ A cm}^{-2}$  to  $0.2 \text{ A cm}^{-2}$  indicates that for the conditions investigated, the added stability from the increase in the air flow rate corresponding to the increase in current density (for constant  $\xi$ ) is mostly offset by the increase in water production. This ability to quantify the effect of operating conditions on dynamical stability associated with cathode water accumulation can be used to stabilize PEFC operation.

Unfortunately, nonlinear noise reduction and computing the correlation sums for invariant estimation are computationally intensive. For instance, on a performance workstation,  $D_2$  and  $K_2$  estimates require at least 10 times the real-time length of the signal using code that has been optimized for computational speed. Thus, the computational time does not make them amenable to real-time, embedded control. Even so, the  $D_2$  and  $K_2$  parameters provide a richness of results that is valuable for post-experimental data analysis and are well-suited to that usage.





**Fig. 10.** a) Correlation dimension and b) Kolmogorov entropy estimates for varying  $\xi$  at constant current densities of 0.1 A cm<sup>-2</sup>, 0.2 A cm<sup>-2</sup>, and 0.3 A cm<sup>-2</sup>. Estimates were weighted by the scaling range, with unweighted  $D_2$  estimates ranging from about 7 to 14. The error bars cover the variability in  $C(r,m)$  over the scaling range.

#### 4.2. Lyapunov exponents

For embedded PEFC control with nonlinear diagnostics, it is vital that the nonlinear signal analysis is not computationally burdensome in order to allow low-cost electronics. As an alternative approach to  $D_2$  and  $K_2$  computation, the unfiltered voltage signals were converted to one-dimensional return maps to evaluate whether the reduced order map of the raw voltage signal maintained some of the chaotic properties of the continuous time state-space attractor of the noise-reduced voltage signal. Voltage peaks were taken to be at least a minimum percentage of the standard deviation of the data above the previous valley (the tolerance), and the Lyapunov exponents of the return map were estimated from the mean divergence of the 50 nearest peaks. For the values reported in Fig. 11, we averaged the LEs computed from peaks over a representative tolerance range of 40%–60%, and the error bars are the standard deviations of the LEs from the same range.

The Lyapunov exponents of the voltage return map in Fig. 11 show the same trend as the rigorous  $D_2$  and  $K_2$  estimates of the time-delay embedded state space. Lyapunov exponents decrease with increasing  $\xi$ , and the curve for 0.1 A cm<sup>-2</sup> is different than that for 0.2 and 0.3 A cm<sup>-2</sup>. Additionally, the LE analysis provides estimates for the conditions at which  $D_2$  and  $K_2$  estimation was not possible due to uncertainty. While the Lyapunov exponents of the voltage return map are reduced-order projections of the Lyapunov exponents from the full state space, the comparison with  $D_2$  and  $K_2$  shows that they capture the relevant stability characteristics of the dynamics and thus are an accurate indication of PEFC stability. The ease of calculation of the map Lyapunov exponents compared to  $D_2$  and  $K_2$  make them excellent candidates for real time stability control, discussed further in Section 5.2.

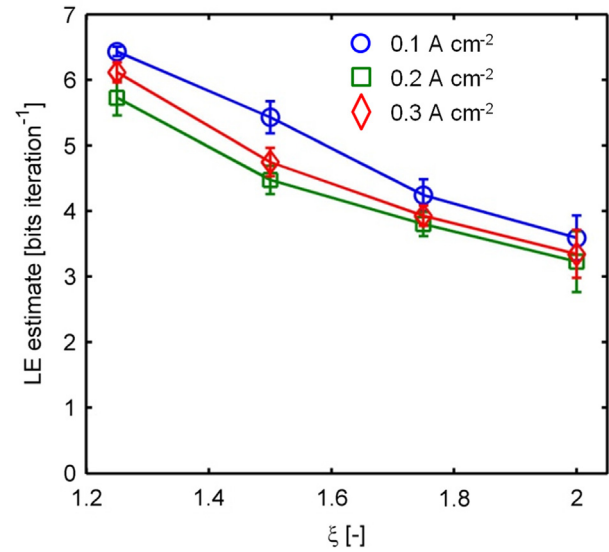


**Fig. 11.** Lyapunov exponent estimates of the voltage return map for varying  $\xi$  at constant current densities of 0.1 A cm<sup>-2</sup>, 0.2 A cm<sup>-2</sup>, and 0.3 A cm<sup>-2</sup>. The estimates are averaged from the mean value of the 50 closest peaks for varying peak tolerances, and the error bars are the standard deviations.

The large standard deviation of the local LE estimates, shown by the error bars in Fig. 11, makes it necessary to include a sufficiently large number of voltage peaks in order to converge to the correct LE value. To determine how many voltage peaks are required, we computed LE estimates for 0.1 A cm<sup>-2</sup> over varying time windows of data. Fig. 12 shows the convergence of the LE estimates for increasing time window sizes, where the shaded error is the standard deviation of the LE estimates of the previous 10 time windows. It can be seen that for time windows >200 s the  $\xi = 1.25$  LE estimate begins to be distinguished from the  $\xi = 1.5$  LE estimate, with convergence to the appropriate value being reached around 300 s. For the less extreme cases of  $\xi = 1.5, 1.75$ , and 2, the LE estimates converge much more quickly and are distinct for all time windows shown.

#### 4.3. Hurst exponents

To gain more insight into how the fuel cell dynamics change with the investigated operating conditions, we used diffusion analysis of 350 s of the raw voltage signals to estimate the Hurst exponents. Fig. 13 shows that for all the conditions, the shortest time windows yield local power law exponents >0.9, indicative of a strong, positive autocorrelation. This can be attributed to the redundancy in the highly-sampled data and the strong determinism over short times. As the time window increases, the local power law exponents decrease until time windows large enough to capture constant power law scaling in the voltage diffusion are used. The power law scaling is limited at the longest time windows by curvature and kinks in the diffusion analysis, which may be spurious artifacts resulting from finite data [30].

The onset of power law scaling, seen as linearity in the log–log plot, as well as the Hurst exponents estimated in the scaling range, are dependent upon operating conditions. The time window length where power law scaling begins is longest for low-current, low- $\xi$  conditions, and decreases with increasing current and  $\xi$  as the dynamical timescales decrease due to increasing air and water flow rates. The Hurst exponent estimates at 0.1 A cm<sup>-2</sup> and low  $\xi$  are close to  $H = 0.5$ , indicating a lack of correlation due to the high entropy and instability in the chaotic dynamics from a significant



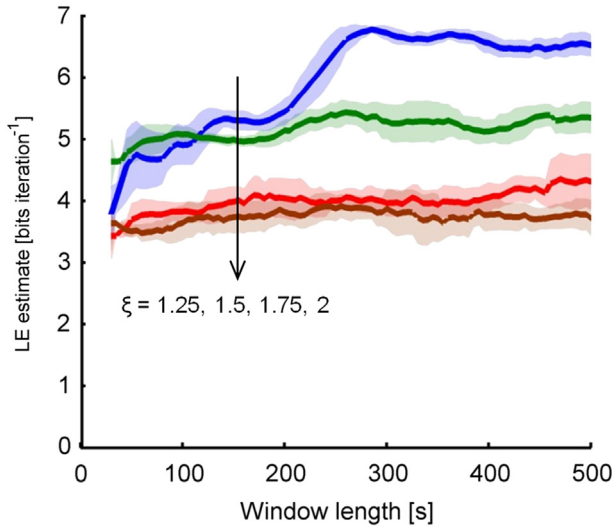


**Fig. 12.** Voltage return map Lyapunov exponent estimates at  $0.1 \text{ A cm}^{-2}$  vs. the time window used for the estimate. The extreme low current/low  $\xi$  case shows that between 200 and 300 s of data are needed to get a conservative 50 peaks with neighbors that accurately represent the dynamics. The shaded error is the standard deviation of the LE estimates of the previous 10 time windows.

amount of water in the cathode. As the current and  $\xi$  increase, the increasing value of  $H$  shows longer autocorrelations as the dynamics gain memory from increasing stability.

In the diffusion analysis, the most chaotic conditions have weak autocorrelations and appear stochastic at sufficiently long time windows, and as the chaos subsides the strength of the autocorrelation increases. Like we observed in the  $D_2$  and  $K_2$  analysis,  $0.2 \text{ A cm}^{-2}$  and  $0.3 \text{ A cm}^{-2}$  show similar behavior exhibited by similar power law scaling, with the exception of  $0.3 \text{ A cm}^{-2}$ ,  $\xi = 2$ . At this condition, no chaotic invariants were estimated and the diffusion analysis reveals a higher  $H$ , indicating a change in dynamical behavior from the transition to a more stable operating regime. The diffusion analysis provides insight into the timescales relevant to PEFC dynamical stability as well as an additional measure of the strength of the stability for the operating conditions

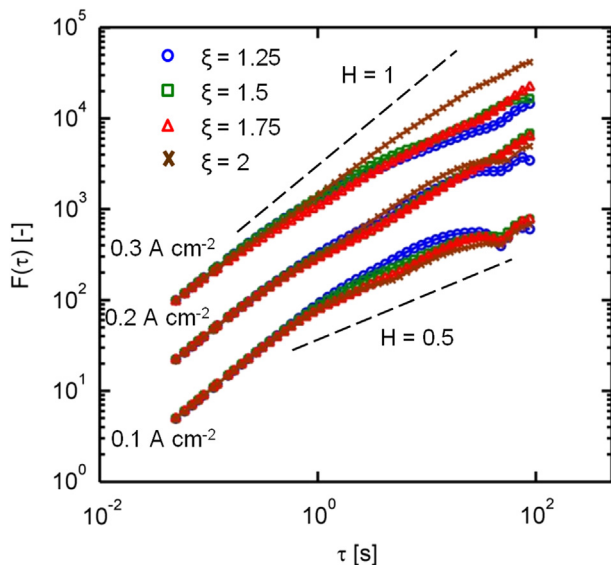


**Fig. 13.** Diffusion analysis for varying  $\xi$  at constant current densities of  $0.1 \text{ A cm}^{-2}$ ,  $0.2 \text{ A cm}^{-2}$ , and  $0.3 \text{ A cm}^{-2}$ . The curves have been vertically separated for clarity.

investigated. Both of these results are important for controller design, discussed further in Section 5.2.

## 5. Discussion

The presence of high-dimensional chaos in low-current, low- $\xi$  PEFC operation indicates the complexity and stability of the dynamics governing cathode water accumulation and removal, including two-phase flow in parallel microchannels. The estimation of invariants  $D_2$  and  $K_2$  is a rigorous way of quantifying experimentally-obtained chaotic PEFC dynamics and the related stability. However, there are some drawbacks, namely the computational power and tuning of parameters required to obtain accurate estimates, that make  $D_2$  and  $K_2$  difficult to compute as part of a quick, robust PEFC water management control scheme. The  $D_2$  and  $K_2$  results presented in this paper inform the development of a reduced-order nonlinear statistic, the Lyapunov exponent of the voltage return map, that provides a first-order approximation of the robust invariants while requiring minimal effort to compute. In this section, we discuss the  $D_2$  and  $K_2$  estimation procedure and its drawbacks, the chaotic dynamics and their relation to cathode water content, and the Lyapunov and Hurst exponents and their applications to active PEFC control.

### 5.1. Chaotic behavior: $D_2$ and $K_2$ estimates

The estimation of chaotic invariants from an experimental time series requires a sufficiently long period of data to populate the attractor to the point where power law scaling is revealed. As the number of degrees of freedom increases, the presence of positive Lyapunov exponents becomes more apparent, making it necessary to obtain exponentially increasing amounts of data to make accurate estimates. To obtain a scaling range of at least a decade, it is estimated that more than  $10^{D_2/2}$  points are required [31]. The unweighted  $D_2$  estimates for the PEFC dynamics studied ranged from about 7 to 14 and required large data sets. Without using the nonlinear noise reduction, our correlation sums showed no power law scaling. Even with the noise reduction, our scaling ranges were very small (less than a decade) and noise still had a significant presence in the voltage signal. However, this is expected for such high-dimensional chaos with a limited amount of data [27]. In addition, the definite power law scaling in the correlation sums (Fig. 4) demonstrates the reliability of our estimates. The observed  $D_2$  trend in Fig. 10 shows an increasing  $D_2$  with decreasing current and  $\xi$ , making it likely that the low-current, low- $\xi$  conditions with no estimates (e.g.  $0.1 \text{ A cm}^{-2}$ ,  $\xi = 1.25$ ) did not have enough data points to reveal the power law scaling. For the missing estimate at the highest current and  $\xi$  tested ( $0.3 \text{ A cm}^{-2}$  and 2, respectively), it is possible that the dynamical behavior changed in the transition to a stable channel flow regime, as it is unlikely that chaotic behavior ceased altogether at this condition. Such a change, which can be seen in the Hurst exponent estimates in Fig. 13, could alter the dimensionality and scaling regions of the attractor, rendering our nonlinear noise reduction parameters ineffective.

As discussed earlier, the presence of noise in the signal has been shown to cause overestimation of  $D_2$  [29]. To better understand the effects of noise on chaotic dynamics, we computed correlation sums from the well-characterized chaotic Lorenz system [20] with superposed white Gaussian measurement and dynamical noise. The correlation sums of the noisy Lorenz system also demonstrated increasing overestimation of  $D_2$  at decreasing scaling ranges. Schreiber has shown that correlation dimensions estimated from correlation sums with measurement noise follow  $D_2(r, m+1) = D_2(r, m) + D_{2, \text{noise}}(r)$  [32]. For Gaussian noise, it can be shown that  $D_{2, \text{Gauss}}(r) = (r \exp(-r^2/4\sigma^2))/(\sigma\sqrt{\pi}\text{erf}(r/2\sigma))$ , a

decreasing function of  $r$  (here  $\sigma$  is the noise amplitude). So, to account for noise in our  $D_2$  and  $K_2$  estimates, we weighted the estimates linearly by the median value of the scaling range, with higher weight given to larger scaling ranges. While the linear weighting is not exact for Gaussian noise, it serves as a first order approximation. This weighting collapsed the  $0.2 \text{ A cm}^{-2}$  and  $0.3 \text{ A cm}^{-2}$   $D_2$  and  $K_2$  estimates onto a single curve while the  $0.1 \text{ A cm}^{-2}$  estimates remained higher (see Fig. 10). The unweighted Lyapunov exponent estimates of the unfiltered voltage return map show a similar trend, Fig. 11, as do the Hurst exponent estimates, Fig. 13, indicating that all of the statistics are describing similar nonlinear phenomena.

The collapse of the  $0.2 \text{ A cm}^{-2}$  and  $0.3 \text{ A cm}^{-2}$  chaotic invariants imply that for this experimental setup, chaotic behavior is more sensitive to changes in air stoichiometric ratio (or superficial gas velocity  $u_g$ ) than to changes in current (or superficial liquid velocity  $u_l$ ) beyond a threshold current density between  $0.1 \text{ A cm}^{-2}$  and  $0.2 \text{ A cm}^{-2}$ . This behavior is indicative of a bifurcation in the dynamics, a nonlinear phenomena whereby the attractor topology will suddenly change, sometimes dramatically, over a smooth change in the system parameters. In a PEFC, such a bifurcation could result from a change in the two-phase flow regime.

As an indicator of the two-phase flow regime, we calculated the two-phase friction factor  $\Phi_{2\phi}$  such that  $\Delta P_{2\phi} = \Delta P_g \Phi_{2\phi}$  where  $\Delta P_g$  was recorded for the dry cathode flow field with no current. Fig. 14 shows the LE estimates versus  $\Phi_{2\phi}$ . The high  $\Phi_{2\phi}$  for the  $0.1 \text{ A cm}^{-2}$  conditions indicates significant two-phase flow effects arising from slug and plug flow when  $u_g$  and  $u_l$  are small. As the current density and  $\xi$  increase,  $\Phi_{2\phi}$  approaches unity and the two-phase effects subside in the transition to a regime with less interaction between phases like the annular/film flow regime. The  $0.1 \text{ A cm}^{-2}$  conditions result in a  $u_l$  value of  $6 \times 10^{-5} \text{ m s}^{-1}$  and  $u_g$  values from  $0.3$  to  $0.5 \text{ m s}^{-1}$  that are well inside the slug flow regime outlined by Hussaini and Wang [4] and exhibit the corresponding high two-phase friction multipliers expected in this flow regime. The high- $\xi$  conditions for the  $0.2$  and  $0.3 \text{ A cm}^{-2}$  conditions result in superficial velocities approaching the transition to film flow, and as expected the two-phase friction multiplier approaches one. At  $0.3 \text{ A cm}^{-2}$  with  $\xi = 1.75$  and  $2$ , the superficial velocities  $u_l$  and  $u_g$  are within the film flow regime bounds measured by Hussaini and Wang and result in two-phase friction multipliers of about one.

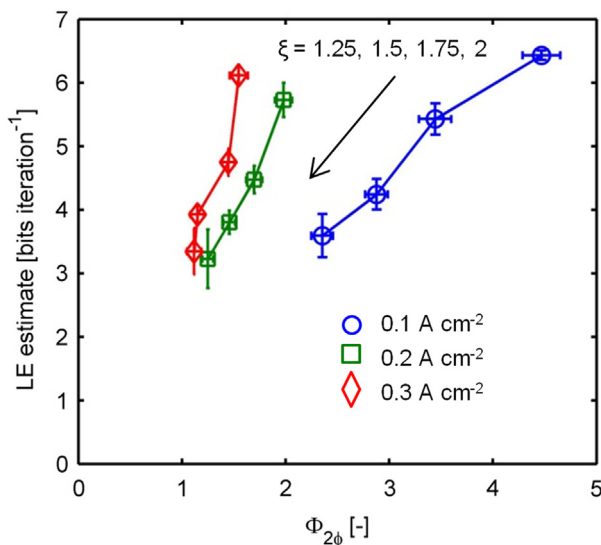


Fig. 14. Two-phase flow regime indication based on  $\Phi_{2\phi}$ . The  $0.1 \text{ A cm}^{-2}$  conditions appear to produce a different flow regime as shown by the high  $\Phi_{2\phi}$ . Convergence to a common LE estimate may be seen as  $\Phi_{2\phi}$  approaches 1.

We see a smooth decrease in  $\Phi_{2\phi}$  during the transition rather than an abrupt change because the product water in a PEFC cathode flow field is introduced along the length of the channel. The water production along the channel causes  $u_l$  to vary along the length of the channel. Thus, for outlet values of  $u_l$  and  $u_g$  near the slug flow to film flow transition, the flow regime can also vary along the length of the channel, yielding a convolution of the distinct flow regime dynamics in the observed, overall dynamics. The relative amount of each regime present in the flow field depends on the proximity of the flow conditions to that of the regime transition. The experimental  $u_g$  and  $u_l$  values for these observations are in accordance with the flow regime map and transitions reported in Ref. [4].

As the two-phase flow effects subside and  $\Phi_{2\phi}$  approaches unity, the LE estimates approach a value around 3, implying the presence of a LE floor due to dynamics unrelated to the two-phase flow. The magnitude of departure from the LE floor with decreasing  $\xi$  has some proportionality to  $\Phi_{2\phi}$ , but we expect that there are also contributions from concentration overpotential. With increasing current density these contributions become more important, and hence we see minimal difference between the LEs for  $0.2$  and  $0.3 \text{ A cm}^{-2}$  even though there are differences in  $\Phi_{2\phi}$  at these conditions. The relationship between the Lyapunov exponents and  $\Phi_{2\phi}$  in Fig. 14 shows that the Lyapunov exponents may be calculated as part of a control scheme to provide information about the cathode water content as it relates to the two-phase flow regime and PEFC dynamical stability, as discussed below.

## 5.2. Control applications: Lyapunov and Hurst exponent estimates

For efficient and effective PEFC water management, there are potentially great benefits from having nonlinear diagnostics indicate the health of operating PEFCs. Control systems based on linear behavior like fluctuation magnitude may take corrective action when none is needed. For example, the standard deviation of the  $0.1 \text{ A cm}^{-2}$ ,  $\xi = 1.75$  voltage signal is about half that of the  $0.3 \text{ A cm}^{-2}$ ,  $\xi = 1.5$  voltage signal (Fig. 8), while the  $D_2$  estimate is greater and the  $K_2$  estimate about the same (Fig. 10). Thus it may prove beneficial to base corrective action on chaotic properties like  $D_2$  and  $K_2$ . However, the estimation procedure for these invariants requires a large number of data points and is computationally expensive, as mentioned earlier, making them unlikely candidates for real-time control.

Instead, we propose using the Lyapunov exponents of the voltage return map to indicate chaotic instability resulting from problematic cathode water accumulation. Elevation of the Lyapunov exponents from a known stable condition, which may vary between fuel cells, shows that the two-phase flow is approaching an unstable regime and corrective action should be taken. Fig. 14 shows that the LE estimates converge to a floor value as the two-phase flow becomes stable, so a stable, reference LE value in a control scheme can be selected from such a plot. Use of the return map reduces the order of the analysis from as many as 14 dimensions to 1 dimension. While such a large reduction of order may eliminate many dynamical properties, we have shown that the Lyapunov exponent estimates of the unfiltered voltage return map follow the same trend as the weighted  $D_2$  and  $K_2$  estimates of the noise-reduced embedded attractor. The average inter-peak intervals used for the return map range from  $0.1 \text{ s}$  (high current and  $\xi$ ) to  $1.7 \text{ s}$  (low current and  $\xi$ ). Hence, the number of time series points used for LE estimation is one to two orders of magnitude less than that used for  $D_2$  and  $K_2$  estimation. Using a conservative  $O(\log n)$  neighborhood search complexity and taking into account the total number of neighborhood searches required, the LE estimation procedure is two to three orders of magnitude faster than the  $D_2$  and  $K_2$  estimation procedure from the reduction in data alone. The

Lyapunov exponents require only seconds of serial computation for estimation, while  $D_2$  and  $K_2$  estimates require hours of parallel processing.

Fig. 1 shows a 300 s time lag between the onset of chaotic behavior and complete voltage shutdown from flooding. In an automotive stack with constantly changing parameters, 300 s might be too large a window to provide effective cathode flooding mitigation. It can be seen in Fig. 12 that most conditions can be distinguished using the LE analysis in as little as 30 s, the shortest time window shown. Furthermore, this analysis uses a conservative 50 peaks for the LE estimate. By implementing a minimum separation for peaks to be considered neighbors, it is possible to achieve an accurate estimate with fewer peaks. When coupled with knowledge of the distributions of local LEs, changes in dynamical behavior could be detected in seconds from a few peaks indicative of the dynamics.

Another candidate metric for chaotic instability detection is the Hurst exponent estimate from the diffusion analysis of the voltage signal. The diffusion analysis in Fig. 13 shows some interesting properties of high-dimensional chaos, as well as relevant time-scales of the dynamics for our PEFC under the operating conditions investigated. In the high-dimensional limit, deterministic chaotic dynamics may appear stochastic [33]. This is due to the positive Lyapunov exponent present in deterministic chaos. Small errors are compounded exponentially quickly, and when many degrees of freedom are present it will cause the dynamics at large enough time windows to appear stochastic. From the diffusion analysis of our PEFC system, we can see that the departure from short-time, ballistic determinism occurs after approximately 1 s. Interestingly, this is also the timescale of the first minimum in the mutual information of the signal, which we used as our embedding time delay, typically around 0.5 s.

The results of the voltage diffusion analysis, specifically the power law scaling transitions between operating conditions and time windows, can be used for PEFC water management. Dynamics are monitored for stochastic behavior at time intervals  $>1$  s, through Hurst exponent estimation or through the use of nonlinear prediction. As the dynamics appear more stochastic, the Hurst exponent will approach 0.5 and the predictability will worsen. When a predefined threshold is crossed, corrective action could be taken.

In future work, the effects of PEFC operating conditions, such as inlet relative humidity and temperature as well as flow field design and wettability should be explored to elucidate their effects on PEFC stability.

## 6. Conclusion

In this research, we have detected the presence of high-dimensional, chaotic dynamics in PEFC operation at low-current, low- $\xi$  conditions typical of startup and idling. The chaotic behavior increases with decreasing current and decreasing  $\xi$ , as the channel  $u_g$  and  $u_l$  move towards those of the two-phase slug flow regime. By weighting our chaotic invariant estimates of dimension and entropy by the median of the state-space power law scaling range to account for noise, we detected bifurcation-like dynamics consistent with a two-phase flow regime transition.

We identified a reduced-order metric indicative of the chaotic behavior. The Lyapunov exponents of the one-dimensional voltage return map capture the chaotic behavior of the high-dimensional reconstructed state space as quantified by the correlation dimension and Kolmogorov entropy. The inclusion of  $>300$  s of data provides an accurate LE estimate for all conditions investigated. For use in a PEFC water management scheme, effective LE estimation from the voltage return map is achievable in seconds.

Using a diffusion analysis to estimate the Hurst exponents of the voltage signal, we have seen how the high-dimensional chaos affects the long-term memory of the PEFC dynamics. More chaotic dynamics have weaker autocorrelations at long times. Detection of stochastic behavior at a time lag  $>1$  s can indicate the level of chaotic behavior and be applied in PEFC control.

## Acknowledgments

This material is based upon work supported by the National Science Foundation under Grant No. 1133025. We gratefully acknowledge Jon Owejan and General Motors for providing the fuel cell materials.

## References

- [1] H. Li, Y. Tang, Z. Wang, Z. Shi, S. Wu, D. Song, J. Zhang, K. Fatih, J. Zhang, H. Wang, Z. Liu, R. Abouatallah, A. Mazza, J. Power Sources 178 (1) (2008) 103–117, <http://dx.doi.org/10.1016/j.jpowsour.2007.12.068>. URL: <http://www.sciencedirect.com/science/article/pii/S0378775307027991>.
- [2] T.A. Zawodzinski, C. Derouin, S. Radzinski, R.J. Sherman, V.T. Smith, T.E. Springer, S. Gottesfeld, J. Electrochem. Soc. 140 (4) (1993) 1041–1047, <http://dx.doi.org/10.1149/1.2056194>. URL: <http://jes.ecsdl.org/content/140/4/1041>.
- [3] T. Trabold, J. Owejan, D. Jacobson, M. Arif, P. Huffman, Int. J. Heat Mass Transfer 49 (25–26) (2006) 4712–4720, <http://dx.doi.org/10.1016/j.ijheat-masstransfer.2006.07.003>. URL: <http://www.sciencedirect.com/science/article/pii/S0017931006004315>.
- [4] I.S. Hussaini, C.-Y. Wang, J. Power Sources 187 (2) (2009) 444–451, <http://dx.doi.org/10.1016/j.jpowsour.2008.11.030>. URL: <http://www.sciencedirect.com/science/article/pii/S0378775308021630>.
- [5] Z. Lu, S.G. Kandlikar, C. Rath, M. Grimm, W. Domigan, A.D. White, M. Hardbarger, J.P. Owejan, T.A. Trabold, Int. J. Hydrogen Energy 34 (8) (2009) 3445–3456, <http://dx.doi.org/10.1016/j.ijhydene.2008.12.025>. WOS: 000266176400026.
- [6] S. Litster, J.G. Santiago, J. Power Sources 188 (1) (2009) 82–88, <http://dx.doi.org/10.1016/j.jpowsour.2008.11.069>. URL: <http://www.sciencedirect.com/science/article/pii/S0378775308021952>.
- [7] J. Owejan, T. Trabold, J. Gagliardo, D. Jacobson, R. Carter, D. Hussey, M. Arif, J. Power Sources 171 (2) (2007) 626–633, <http://dx.doi.org/10.1016/j.jpowsour.2007.06.174>. URL: <http://www.sciencedirect.com/science/article/pii/S0378775307014693>.
- [8] N.S. Siefert, S. Litster, J. Power Sources 196 (4) (2011) 1948–1954, <http://dx.doi.org/10.1016/j.jpowsour.2010.10.026>. URL: <http://www.sciencedirect.com/science/article/pii/S0378775310017532>.
- [9] D.L. Wood III, J.S. Yi, T.V. Nguyen, Electrochim. Acta 43 (24) (1998) 3795–3809, [http://dx.doi.org/10.1016/S0013-4686\(98\)00139-X](http://dx.doi.org/10.1016/S0013-4686(98)00139-X). URL: <http://www.sciencedirect.com/science/article/pii/S001346869800139X>.
- [10] F.Y. Zhang, X.G. Yang, C.Y. Wang, J. Electrochem. Soc. 153 (2) (2006) A225, <http://dx.doi.org/10.1149/1.2138675>. URL: <http://link.aip.org/link/JESOA/v153/i2/pA225/s1&Agg=doi>.
- [11] J. Owejan, T. Trabold, D. Jacobson, M. Arif, S. Kandlikar, Int. J. Hydrogen Energy 32 (17) (2007) 4489–4502, <http://dx.doi.org/10.1016/j.ijhydene.2007.05.044>. URL: <http://www.sciencedirect.com/science/article/pii/S0360319907003357>.
- [12] I.D. Chapman, C. MacKintosh, P.A. Rapaport, Fluid flow pulsing for increased stability in PEM fuel cell, Publication Number: US 2005/0260463 A1 U.S. Classification: 429/432 International Classification: H01M008/04. URL: <http://www.google.com/patents?id=tu6UAAAEBAJ>.
- [13] A.M. Niroumand, W. Mérida, M. Saif, J. Process Control 21 (4) (2011) 602–612, <http://dx.doi.org/10.1016/j.jprocont.2010.12.013>. URL: <http://www.sciencedirect.com/science/article/pii/S0959152410002660>.
- [14] W. Mérida, D. Harrington, J. Le Canut, G. McLean, J. Power Sources 161 (1) (2006) 264–274, <http://dx.doi.org/10.1016/j.jpowsour.2006.03.067>. URL: <http://www.sciencedirect.com/science/article/pii/S0378775306005982>.
- [15] J.-C. Roux, R.H. Simoyi, H.L. Swinney, Phys. D Nonlinear Phenom. 8 (1–2) (1983) 257–266, [http://dx.doi.org/10.1016/0167-2789\(83\)90323-8](http://dx.doi.org/10.1016/0167-2789(83)90323-8). URL: <http://www.sciencedirect.com/science/article/pii/0167278983903238>.
- [16] S. Nedeltchev, U. Jordan, O. Lorenz, A. Schumpe, Chem. Eng. Technol. 30 (4) (2007) 534–539, <http://dx.doi.org/10.1002/ceat.200600344>. URL: <http://onlinelibrary.wiley.com/doi/10.1002/ceat.200600344/abstract>.
- [17] C.M. van den Bleek, M.-O. Coppens, J.C. Schouten, Chem. Eng. Sci. 57 (22–23) (2002) 4763–4778, [http://dx.doi.org/10.1016/S0009-2509\(02\)00288-9](http://dx.doi.org/10.1016/S0009-2509(02)00288-9). URL: <http://www.sciencedirect.com/science/article/pii/S0009250902002889>.
- [18] E. Ott, C. Grebogi, J.A. Yorke, Phys. Rev. Lett. 64 (11) (1990) 1196–1199, <http://dx.doi.org/10.1103/PhysRevLett.64.1196>. URL: <http://link.aps.org/doi/10.1103/PhysRevLett.64.1196>.
- [19] P. Parmananda, P. Sherard, R.W. Rollins, H.D. Dewald, Phys. Rev. E 47 (5) (1993) R3003–R3006, <http://dx.doi.org/10.1103/PhysRevE.47.R3003>. URL: <http://link.aps.org/doi/10.1103/PhysRevE.47.R3003>.

- [20] E.N. Lorenz, *J. Atmos. Sci.* 20 (2) (1963) 130–141, [http://dx.doi.org/10.1175/1520-0469\(1963\)020<0130:DNF>2.0.CO;2](http://dx.doi.org/10.1175/1520-0469(1963)020<0130:DNF>2.0.CO;2). URL: [http://journals.ametsoc.org/doi/abs/10.1175/1520-0469\(1963\)020%3C0130%3ADNF%3E2.0.CO%3B2](http://journals.ametsoc.org/doi/abs/10.1175/1520-0469(1963)020%3C0130%3ADNF%3E2.0.CO%3B2).
- [21] F. Takens, in: D. Rand, L.-S. Young (Eds.), *Dynamical Systems and Turbulence*, Warwick 1980, Vol. 898 of *Lecture Notes in Mathematics*, Springer, Berlin/Heidelberg, 1981, pp. 366–381. URL: <http://www.springerlink.com/content/b254x77553874745/abstract/>.
- [22] P. Grassberger, R. Hegger, H. Kantz, C. Schaffrath, T. Schreiber, *J. Nonlinear Sci.* 3 (2) (1993) 127–141, <http://dx.doi.org/10.1063/1.165979>. URL: [http://chaos.aip.org/resource/1/chaoeh/v3/i2/p127\\_s1](http://chaos.aip.org/resource/1/chaoeh/v3/i2/p127_s1).
- [23] P. Grassberger, I. Procaccia, *Phys. D Nonlinear Phenom.* 9 (1–2) (1983) 189–208, [http://dx.doi.org/10.1016/0167-2789\(83\)90298-1](http://dx.doi.org/10.1016/0167-2789(83)90298-1). URL: <http://www.sciencedirect.com/science/article/pii/0167278983902981>.
- [24] P. Grassberger, I. Procaccia, *Phys. Rev. A* 28 (4) (1983) 2591–2593, <http://dx.doi.org/10.1103/PhysRevA.28.2591>. URL: <http://link.aps.org/doi/10.1103/PhysRevA.28.2591>.
- [25] H. Hurst, *Trans. Am. Soc. Civil Eng.* 116 (1951) 770–808.
- [26] D. Grech, Z. Mazur, *Phys. A Stat. Mech. Appl.* 336 (1–2) (2004) 133–145, <http://dx.doi.org/10.1016/j.physa.2004.01.018>. URL: <http://www.sciencedirect.com/science/article/pii/S037843710400041X>.
- [27] H. Kantz, T. Schreiber, *Nonlinear Time Series Analysis*, Cambridge University Press, 2004.
- [28] J.P. Owejan, J.J. Gagliardo, J.M. Sergi, S.G. Kandlikar, T.A. Trabold, *Int. J. Hydrogen Energy* 34 (8) (2009) 3436–3444, <http://dx.doi.org/10.1016/j.ijhydene.2008.12.100>. URL: <http://www.sciencedirect.com/science/article/pii/S0360319909000366>.
- [29] M. Ding, C. Grebogi, E. Ott, T. Sauer, J.A. Yorke, *Phys. D Nonlinear Phenom.* 69 (3–4) (1993) 404–424, [http://dx.doi.org/10.1016/0167-2789\(93\)90103-8](http://dx.doi.org/10.1016/0167-2789(93)90103-8). URL: <http://www.sciencedirect.com/science/article/pii/0167278993901038>.
- [30] R.M. Bryce, K.B. Sprague, *Sci. Rep.* 2, <http://dx.doi.org/10.1038/srep00315>. URL: <http://www.nature.com/srep/2012/120314/srep00315/full/srep00315.html>.
- [31] J.-P. Eckmann, D. Ruelle, *Phys. D Nonlinear Phenom.* 56 (2–3) (1992) 185–187, [http://dx.doi.org/10.1016/0167-2789\(92\)90023-G](http://dx.doi.org/10.1016/0167-2789(92)90023-G). URL: <http://www.sciencedirect.com/science/article/pii/016727899290023G>.
- [32] T. Schreiber, *Phys. Rev. E* 48 (1) (1993) R13–R16, <http://dx.doi.org/10.1103/PhysRevE.48.R13>. URL: <http://link.aps.org/doi/10.1103/PhysRevE.48.R13>.
- [33] M. Casdagli, *J. Royal Stat. Soc. Ser. B (Methodological)* 54 (2) (1992) 303–328, <http://dx.doi.org/10.2307/2346130>. Article Type: research-article/Full publication date: 1992/Copyright ©1992 Royal Statistical Society. URL: <http://www.jstor.org/stable/2346130>.